The stratification of seismic azimuthal anisotropy in the western US

Fan-Chi Lin[1], Michael H. Ritzwoller[1], Yingjie Yang[1], Morgan P. Moschetti[1], and Matthew J. Fouch[2]

1 - Center for Imaging the Earth's Interior, Department of Physics, University of Colorado at Boulder, Boulder, CO
2 - School of Earth and Space Exploration, Arizona State University, Tempe, AZ

One-sentence summaries

Innovations in the observation of broad-band surface waves allow the inference of 3D azimuthal anisotropy within the crust, lithosphere, and asthenosphere beneath the western US at geological length-scales, which provides new constraints on crustal and mantle deformation, crust-mantle coupling, and sub-lithospheric mantle flow.

Abstract

Short to intermediate period (12 to 54 s) Rayleigh wave phase travel times and SKS shear wave splitting measurements observed with the EarthScope USArray in the western US are used to estimate the 3D distribution of azimuthal anisotropy. The inferred stratified model of anisotropy consists of a middle-to-lower crustal layer, a 80 km thick uppermost mantle layer, and a 200 km thick smoothly varying asthenospheric mantle layer. The pattern of crustal anisotropy relates well to major geological provinces but is uncorrelated with anisotropy in the uppermost mantle and asthenosphere. The fast axis directions in the underlying asthenosphere separate coherently into three broad tectonic regions: the tectonically active western US including the Basin and Range Province, the Columbia Basin, and much of California, the more tectonically stable regions east of 113°E longitude including the Colorado Plateau, and the Cascadia subduction system. The inferred stratification of anisotropy suggests complex and highly variable crust-mantle mechanical

coupling in the western US. Observations of complex regional azimuthal anisotropy are therefore dominated by relatively shallow, regional-scale tectonic processes, and the more homogeneous deeper mantle anisotropy pattern reveals a mantle flow field controlled by a combination of North American plate motion and the subduction of the Juan de Fuca / Farallon slab system.

Knowledge of the stratification of anisotropy in the crust and uppermost mantle is critical to an understanding of strain partitioning within and at the base of the continental lithosphere, which in turn would illuminate the dynamical coupling within and at the base of tectonic plates. Seismic anisotropy within the upper mantle appears ubiquitously, but is correlated with diverse dynamical causes. In some continental regions, anisotropy inferred by shear wave splitting measurements is correlated with surface geological features, which may provide evidence that anisotropy is predominantly a lithospheric phenomenon (Silver, 1996) and may be frozen in at the time of formation or subsequent lithospheric deformation. In other regions, anisotropy appears more closely aligned with absolute plate motions (Vinnik et al. 1992), suggesting that anisotropic fabric reflects sublithospheric flows and may still be evolving. Many regions exist where a combination of lithospheric and asthenospheric fabric best explains observed anisotropy (e.g., Fouch et al., 2000). It has not been possible, however, to produce an integrated model of anisotropy of the lithosphere and the underlying asthenosphere (Marone and Romanowicz, 2007), preferably derived from more than one type of observable. Because shear wave splitting provides a path-integrated measurement beneath seismic receivers, the depth resolution of splitting measurements is poor. Surface waves provide complementary information about azimuthal anisotropy, but teleseismic observations at periods that uniquely constrain the crust (<20 sec) are rare and shear wave splitting measurements and surface wave models of azimuthal

anisotropy frequently do not agree well (Montagner et al., 2000; Debayle et al., 2005). Recent advances in surface wave methodology, particularly the development of the method of ambient noise tomography (Sabra et al., 2005; Shapiro et al., 2005), improvements in earthquake tomography (Yang and Forsyth, 2006; Yang et al., 2008), and the ongoing deployment of the USArray Transportable Array (TA) stations (Fig 1a) in the western US, have dramatically improved information recovered about anisotropy in the shallow earth and allow for the development of an integrated high resolution model of azimuthal anisotropy in the crust, lithospheric mantle, and underlying asthenosphere.

In this study, we obtain Rayleigh wave phase travel time measurements at periods from 12 to 54 sec to infer the azimuthal anisotropy in the crust and uppermost mantle and, combined with SKS splitting measurements (West et al. 2009; Fouch and West, in prep., 2010), apply new constraints on the azimuthal anisotropy within the asthenospheric mantle. We measure Rayleigh wave travel times using ambient noise (Bensen et al., 2007) at periods from 12 to 46 sec using waveforms observed at 611 TA stations that operated between Oct 2004 and Oct 2008 (Lin et at., 2008). Similar measurements from 24 to 54 sec period are obtained from 574 teleseismic earthquakes with Ms $\geq$ 5.0 that occurred between Jan 2006 and Jan 2009. The principal tomographic method used, called Eikonal tomography (Lin et al., 2009), involves empirical phase front tracking (Pollitz, 2008) to estimate azimuthally dependent phase velocity and its uncertainty on a 0.2° spatial grid (Fig 1b-g) by calculating the gradient across each phase travel time surface. At each location, velocity measurements from ambient noise and earthquake tomography are averaged in the period band of overlap. Eikonal tomography takes advantage of the contemporaneous array of stations and complements traditional surface wave tomography in several ways: there is no explicit regularization, it accounts for ray bending, it generates error estimates in the inferred

dispersion maps for both isotropic and anisotropic parameters, and the azimuthal anisotropy signal can be visually and numerically inspected at each spatial node.

Based on observations of the 180° azimuthal periodicity of Rayleigh wave speeds (Fig. 1b-g), we adopt the 2-psi functional form for a weakly anisotropic medium (Smith and Dahlen, 1973) and parameterize the observed azimuthal anisotropy at each period and location with a fast direction and anisotropy amplitude. The robustness of the observed anisotropy patterns as well as estimates of their uncertainty (Note N1) is verified by comparing the independent results obtained from the ambient noise and earthquake datasets (Fig. S1). Because more earthquake measurements are accepted at long periods and more ambient noise measurements at short periods, averaging effectively weights up earthquake measurements at long periods and ambient noise at short periods. At periods above 54 sec, finite frequency effects degrade the reliability of azimuthal anisotropy information from surface waves (Bodin & Maupin 2008).

Fig. 2a-c summarizes the observations of Rayleigh wave azimuthal anisotropy at periods of 12, 26, and 38 sec, which are most sensitive to anisotropy in the middle crust, lower crust and uppermost mantle, and uppermost mantle, respectively. Clear differences in the patterns of anisotropy between 12 and 38 sec period require the stratification of anisotropy between the crust and uppermost mantle. Fig 2d-e exemplifies the period dependence of the fast azimuths and anisotropy amplitudes, which we refer to as anisotropic dispersion curves, for a point in northern Nevada (star in Fig 1a) where the fast directions at short (<18 s) and long (>32 s) periods are stable but differ from one another. Based on these anisotropic dispersion curves at each location, we invert for a 3D azimuthally anisotropic shear velocity model in the crust and uppermost mantle. First, we follow the method of Moschetti *et al.* (2010) to construct a reference isotropic

model represented with four crustal layers and five B-splines in the upper mantle. Shear wave anomalies in the isotropic model (e.g., Fig. 3a-b) correspond to major geological features and are consistent with a previous study (Yang et al. 2008). Second, we introduce azimuthal anisotropy perturbations to the isotropic model to fit the anisotropic dispersion curves observed at each location. Most observed anisotropic dispersion curves are well fit by a two-layer model (Fig2d-e; Fig. S2) in which azimuthal anisotropy is introduced in the middle-to-lower crust and the uppermost mantle roughly approximating the lithosphere. Anisotropy in each layer is vertically constant but laterally variable. The depth extent of the uppermost mantle layer is not constrained beneath 100 km depth where the surface wave data lose their sensitivity. The crustal and uppermost mantle anisotropic models are summarized in Fig 3a-b and the estimated model uncertainties are presented in Fig. S3.

By comparing model predicted and observed SKS splitting measurements within the western US, we can constrain the thickness of the uppermost mantle layer as well as azimuthal anisotropy in the underlying asthenospheric mantle. We use the method described by Rumpker & Silver (1998) to synthesize the azimuthally averaged SKS apparent splitting parameters from our model and calculate the misfit between the model predicted and observed SKS splitting measurements (Supplementary Material SM1). To avoid over parameterization, we assume laterally constant uppermost mantle thickness and asthenospheric splitting strength and only allow smooth lateral variations of asthenospheric fast directions (Note N2). The misfit minimizes when the uppermost mantle layer extends to a depth of 80 km below the Moho, the splitting time of the asthenospheric layer is 0.8 s, and the fast directions of the layer as shown in Fig. 3c. Uncertainties in the asthenospheric fast axis directions average ~6° across the study region and are shown in Fig S4. This results in our preferred or final three-layer anisotropy model,

where Fig. 3d summarizes the predicted SKS apparent splitting parameters and Fig. 4a-c present comparisons with the observations. Misfit statistics to the surface wave anisotropic dispersion curves and to the SKS data for our final model (Model C) and two others (Model A: a two-layer crust/uppermost mantle model in which the upper mantle layer extends to 220 km beneath the Moho; Model B: a three-layer model in which the asthenospheric layer is laterally invariant) are presented in Table 1. A 64% variance reduction to the SKS observation is achieved relative to an isotropic model by our preferred model. Differences in fast directions and split times are summarized with histograms in Fig. 4b-c, with the standard deviation of the directional difference equal to 18°, in good agreement with differences expected from model and data uncertainties. About 80% of the model predictions agree with the SKS fast directions by better than 20º, although the final model under-predicts split times by 0.25 sec, on average. To contrast with Fig. 4, comparison between the SKS observations and predictions from Models A and B are shown in Figs. S5 and S6.

The crustal and uppermost mantle anisotropy layers, which are constrained exclusively by the surface wave data and possess a lateral resolution of ~200 km (Lin et al. 2009), provides information about the spatial variability of anisotropy on scales similar to the major geological and tectonic features across this region. Significant variations in fast directions are observed both in the crust and uppermost mantle (Fig. 3a-b) with a particularly strong coherence between the crustal anisotropy pattern, isotropic structures, and the major geological provinces. This includes N-S fast directions across nearly the entire Basin and Range province coincident with the region of strong crustal radial anisotropy (Moschetti *et al. 2010*), NW-SE fast directions within the Central Valley of California, E-W fast directions within the Cascadia forearc roughly parallel to the subduction direction of the Juan de Fuca Plate, NE-SW fast directions within the Colorado

Plateau, E-W fast directions within the High Lava Plains, and weak anisotropy within the Snake River Plain. Spatial patterns of anisotropy within the uppermost mantle, on the other hand, are neither well correlated with surface geological features nor with the crustal anisotropy pattern (Fig. 4d). The directional correlation coefficient between the crustal and uppermost mantle fast axis distributions is found to be **r** = 0.12, and a Monte Carlo simulation shows that 1 out of 4 random directional distribution pairs correlate at least as well (Supplementary Materials SM2).

Within the uppermost mantle, strong anisotropy is observed both near the western and eastern boundaries of the Great Basin, although the fast directions are rotated almost 90°. Near the western boundary of the Great Basin, the east-west oriented fast directions are coherent across a broader region, which extends northward into the High Lava Plains province. As with the eastern boundary, the strong anisotropy coincides with slow isotropic anomalies in the uppermost mantle. Near the western plate boundaries, anisotropic fast directions change abruptly near the Mendocino Triple Junction, consistent with a change in the principal stress direction from a strike-slip related system to the south to a subduction related system to the north. Similar to crustal anisotropy, weak uppermost mantle anisotropy is observed beneath the Snake River Plain. The average strength of uppermost mantle anisotropy across the whole study area is ~1.3% which is slightly stronger than ~1.1% anisotropy observed in the crust. The strength of anisotropy, however, probably is underestimated due to the diminishment of anisotropy amplitudes near regions where fast directions change abruptly laterally.

In contrast with the patterns of anisotropy within the crust and uppermost mantle that vary on geological scales, the azimuthal anisotropy pattern observed within the deeper layer (Fig. 3c) is probably attributable to large-scale asthenospheric flow beneath most regions of the western US.

By assuming an anisotropic strength of 2% in this layer, the 0.8 sec splitting time implies a thickness of about 200 km beneath the uppermost mantle layer (i.e., below ~110 km depth). The fast directions of the observed asthenospheric anisotropy, although smoothly varying, can be approximately separated into three major tectonic regions. In the east, the fast directions (blue shaded in Fig. 3c) average about 32° (±12°) N of E, matching the direction of absolute plate motion (33° S of W, Gripp & Gordon 2002) beneath the North American craton. In the west, nearly E-W fast directions are observed in most of the tectonically active western US, which may be induced by a combination of absolute plate motions and the geodynamic effect of the previously subducted Farallon slab (Silver & Holt 2002; Becker et al. 2006), as well as rapid eastward inflow of Pacific asthenosphere in the gap between the Mendocino and Rivera Triple Junctions where subduction has been eradicated. North of the Mendocino Triple Junction within Cascadia, a distinct region with fast directions nearly parallel to the NE-directed subduction of Juan de Fuca plate (Fig. 1a) is observed.

Our final 3D model of stratified azimuthal anisotropy reconciles surface wave observations and SKS splitting measurements to within expectations based on data uncertainties and model resolution. This model of anisotropy of the crust, uppermost mantle, and asthenosphere provides new constraints on strain partitioning within the crust and upper mantle and on geodynamical models of deformation within and beneath the lithosphere. Anisotropic features within the crust correlate well with large-scale geological provinces. The disagreement between the patterns of anisotropy in the crust and uppermost mantle argues against a model of simple mechanical coupling between these layers, which has been suggested for regions of thicker lithosphere (Holt 2000) and provides a challenge for lithospheric modeling. In the uppermost mantle, although anisotropy in regions associated with fast isotropic wave speeds (i.e., cold regions) may be

"frozen-in", anisotropy in regions with slow isotropic wave speeds may be evolving with the current sub-crustal deformation. A weak directional agreement is observed between the uppermost mantle and asthenospheric layers (Fig. 4e), where uppermost mantle and asthenospheric fast axis directions align predominantly in regions of slow (i.e., hot) upper mantle where the lithosphere is thinnest: in the western Basin and Range, the High Lava Plains, and in Cascadia. In particular, correlations between strong anisotropy and slow upper mantle isotropic wave speed anomalies are observed near the High Lava Plains where large SKS splitting times exist (Long et al. 2009), and in western Utah where an enigmatic N-S SKS fast polarization pattern has been imaged (Savage & Sheehan 2000; Zandt & Humphreys 2008; West et al, 2009). As expected based on our model parameterization in which smaller (<300 km) lateral variations in asthenospheric anisotropy are not resolved, zones of sharp reductions in shear wave splitting times, such as is found in the central Great Basin and interpreted as a ~150-km wide zone of mantle downwelling (West et al. 2009), do not appear in our model. Fast directions parallel to the San Andreas Fault in the uppermost mantle near the North American plate boundary can be explained by assuming that the olivine fast axis [100] aligns with the deformation direction induced by simple shear (Zhang & Karato 1995). E-W asthenospheric fast directions in this area suggest that plate interaction deformation does not penetrate significantly at asthenospheric depths. This is consistent with previous SKS splitting studies near the San Andreas Fault, where azimuthally dependent apparent splitting parameters were studied (Savage & Silver 1993; Ozalaybey & Savage 1995). Numerous studies have used shear wave splitting measurements to infer sub-lithospheric flow beneath the western US (e.g. see Savage 2002 for review; Sheehan et al. 1997; Savage and Sheehan, 2000; Silver & Holt 2002; Becker et al. 2006; Zandt & Humphreys 2008; West et al, 2009). The spatial pattern of broad-scale asthenospheric

anisotropy in our final model reconciles earlier studies that have suggested that sub-lithospheric anisotropy is induced by absolute plate motions (Marone & Romanowicz 2007) and the subduction of the Juan de Fuca and Farallon slabs (Silver & Holt 2002; Becker et al. 2006; Zandt & Humphreys 2008).

Acknowledgments

Instruments [data] used in this study were made available through EarthScope (www.earthscope.org; EAR-0323309), supported by the National Science Foundation. The facilities of the IRIS Data Management System, and specifically the IRIS Data Management Center, were used for access to waveform and metadata required in this study. The IRIS DMS is funded through the National Science Foundation and specifically the GEO Directorate through the Instrumentation and Facilities Program of the National Science Foundation under Cooperative Agreement EAR-0552316. This work has been supported by NSF grants EAR-0711526 and EAR-0844097.

References

Silver, P.G. Seismic anisotropy beneath the continents: Probing the depths of geology, *Annu. Rev. Earth Planet. Sci.* **24**, 385-342 (1996).

Vinnik, L.P., Makeyeva, L.I., Milev, A., & Ushenko, A.Y. Global patterns of azimuthal anisotropy and deformations in the continental mantle, *Geophys. J. Int.* **111**, 433-447 (1992).

Fouch, M.J., Fischer, K.M., Wysession, M.E., & Clarke, T.J. Shear wave splitting, continental keels, and patterns of mantle flow, *J. Geophys. Res.* **105**, 6255-6276 (2000).

Marone, F. & Romanowicz, B. The depth distribution of azimuthal anisotropy in the continental upper mantle, *Nature* **447**, 198-201 (2007).

Montagner, J.-P., Griot-Pommera, D.-A., & Lave, J. How to reltae body wave and surface wave anisotropy?, *J. Geophys. Res.* **105**, 19015-19027 (2000).

Debayle, E., Kennett, B.L.N., & Priestley, K. Global azimuthal seismic anisotropy and the unique plate-motion deformation of Australia, *Science* **433**, 509-512 (2005).

Sabra, K. G., Gerstoft, P., Roux, P., Kuperman, W. A. & Fehler, M. C. Surface wave tomography from microseisms in Southern California. *Geophys. Res. Lett.* **32**, L14311 (2005).

Shapiro, N. M., Campillo, M., Stehly, L. & Ritzwoller, M. H. High-resolution surface-wave tomography from ambient seismic noise. *Science* **307**, 1615-1618 (2005).

Yang, Y. & Forsyth, D. W. Rayleigh wave phase velocities, small-scale convection, and azimuthal anisotropy beneath southern California. *Journal of Geophysical Research-Solid Earth* **111**, B07306 (2006).

Yang, Y., Ritzwoller, M. H., Lin, F. -., Moschetti, M. P. & Shapiro, N. M. Structure of the crust and uppermost mantle beneath the western United States revealed by ambient noise and earthquake tomography. *J. Geophys. Res. -Solid Earth* **113**, B12310 (2008).

West, J. D., Fouch, M. J., Roth, J. B. & Elkins-Tanton, L. T. Vertical mantle flow associated with a lithospheric drip beneath the Great Basin. *Nat. Geosci.* **2**, 438-443 (2009).

Fouch, M. J. & West, J. D. The mantle flow field beneath the western United States, in preparation.

Bensen, G. D. *et al*. Processing seismic ambient noise data to obtain reliable broad-band surface wave dispersion measurements. *Geophysical Journal International* **169**, 1239-1260 (2007).

Lin, F. C., Moschetti, M. P. & Ritzwoller, M. H. Surface wave tomography of the western United States from ambient seismic noise: Rayleigh and Love wave phase velocity maps. *Geophysical Journal International* **173**, 281-298 (2008).

Lin, F., Ritzwoller, M. H. & Snieder, R. Eikonal tomography: surface wave tomography by phase front tracking across a regional broad-band seismic array. *Geophys. J. Int.* **177**, 1091-1110 (2009).

Pollitz, F. F. Observations and interpretation of fundamental mode Rayleigh wavefields recorded by the Transportable Array (USArray). *J. Geophys. Res. -Solid Earth* **113**, B10311 (2008).

Smith, M. L. & Dahlen, F. A. Azimuthal Dependence of Love and Rayleigh-Wave Propagation in a Slightly Anisotropic Medium. *Journal of Geophysical Research* **78**, 3321-3333 (1973).

Bodin, T. & Maupin, V. Resolution potential of surface wave phase velocity measurements at small arrays. *Geophys. J. Int.* **172**, 698-706 (2008).

Moschetti, M. P., Ritzwoller, M. H., & Lin, F.-C. Seismic evidence for widespread deep crustal deformation caused by extension in the western US. *Nature*, in press (2010).

Rumpker, G. & Silver, P. G. Apparent shear-wave splitting parameters in the presence of vertically varying anisotropy. *Geophysical Journal International* **135**, 790-800 (1998).

Gripp, A. E. & Gordon, R. G. Young tracks of hotspots and current plate velocities. *Geophys. J. Int.* **150**, 321-361 (2002).

Silver, P. & Holt, W. (2002). The mantle flow field beneath western North America. *Science*, 295(5557), 1054–1057.

Becker, T. W., Schulte-Pelkum, V., Blackman, D. K., Kellogg, J. B. & O'Connell, R. J. Mantle flow under the western United States from shear wave splitting. *Earth Planet. Sci. Lett.* **247**, 235-251 (2006).

Holt, W. E. Correlated crust and mantle strain fields in Tibet. *Geology* **28**, 67-70 (2000).

Long, M.D., Gao, H., Klaus, A., Wagner, L.S., Fouch, M.J., James, D.E., & Humphreys, E. Shear wave splitting and the pattern of mantle flow beneath eastern Oregon, *Earth Planet Sci. Lett.* **288**, 359-369 (2009)

Savage, M. K. & Sheehan, A. F. Seismic anisotropy and mantle flow from the Great Basin to the Great Plains, western United States. *Journal of Geophysical Research-Solid Earth* **105**, 13715-13734 (2000).

Zandt, G. & Humphreys, E. Toroidal mantle flow through the western US slab window. *Geology* **36**, 295-298 (2008).

Zhang, S. Q. & Karato, S. Lattice preferred orientation of olivine aggregates deformed in simple shear. *Nature* **375**, 774-777 (1995).

Savage, M. K. & Silver, P. G. (1993). Mantle deformation and tectonics – constraints from seismic anisotropy in the western United-States. *Phys. Earth Planet. Int.*, 78(3-4), 207–227.

Ozalaybey, S. & Savage, M. K. Shear-Wave Splitting Beneath Western United-States in Relation to Plate-Tectonics. *Journal of Geophysical Research-Solid Earth* **100**, 18135-18149 (1995).

Savage, M. K. Seismic anisotropy and mantle deformation in the western United States and southwestern Canada. *Int. Geol. Rev.* **44**, 913-937 (2002).

Notes

N1. Lin *et al.* 2009 discuss the estimation of uncertainty for the two anisotropic dispersion parameters (period dependent fast axis direction and amplitude) shown, for example, in Fig. 2d-e. To prevent underestimation of uncertainties, two additional uncertainty scaling schemes are applied. First, the reduced chi-squared value of the best fitting 2-psi curve, χ^2, is used to scale the uncertainty of both parameters by $\lambda=\exp(\chi^2/6)$. The effect is to scale up uncertainties at periods where data misfit is large. Second, if the anisotropy amplitude, *c*, is less than 0.75% we scale the fast direction uncertainty by $\lambda = 8.5-10c$, which acts to diminish the effect of fast direction measurements where amplitudes are small in the ensuing inversion.

N2. In order to ensure only smooth lateral variations of asthenospheric fast directions, for each location we minimize the misfit between the predicted and observed SKS measurements within 300 km by assuming a constant fast direction in the asthenospheric layer. The tradeoff between splitting strength in the asthenospheric layer and the thickness of the uppermost mantle layer increases the difficulty of investigating the spatial variation of these two parameters. This smoothing process effectively down weights the effect of small scale variations in the SKS measurements.

Figure Captions

Figure 1.

(a) Maps of the study region where black triangles identify the seismic stations used, which are mainly from the EarthScope USarray Transportable Array. Major tectonic boundaries are drawn with red lines and the plate boundaries with yellow lines. Black arrows indicate the relative motions between the Pacific (PA) and North American Plates (NA), the Juan de Fuca Plate (JdF) and NA, and NA and the hotspot reference frame (HS) (Gripp & Gordon, 2002). Red stars mark the locations of examples shown in Fig. 1b-g and Fig. 2d-e. (b)-(g) Examples of 12, 26, and 38 sec period Rayleigh wave azimuthally dependent phase velocity measurements in northern Nevada and western Utah. Green dashed lines are the best fitting 2-psi variation curves, which are used to estimate both the fast direction and the amplitude of anisotropy with their uncertainties.

Figure 2.

(a)-(c) Maps of 12, 26, and 38 sec period Rayleigh wave azimuthal anisotropy on a 0.6° spatial grid. The fast propagation direction and anisotropic amplitude are presented by the orientation and length of the red bars. (d)-(e) An example of anisotropy dispersion curves for a location in northern Nevada between periods of 12 and 54 sec with associated uncertainties. The red lines are the best fitting dispersion curves based on the crustal and uppermost mantle model shown in Fig. 3a-b.

Figure 3.

(a)-(c) Anisotropic properties of the middle-to-lower crust, uppermost mantle, and asthenosphere in our final model, where the fast propagation direction and anisotropic amplitude are represented by the orientation and length of the yellow/red bars on a 0.6° spatial grid. Isotropic shear wave speeds at depths of 15 and 50 km are color coded in the background of (a)-(b), and the fast direction is shown in the background in (c). (d) The predicted SKS measurements based on the 3D anisotropic model, where the fast direction and splitting time are represented by the orientation and length of the red bars on a 0.6° spatial grid. The splitting time is also color coded in the background.

Figure 4.

(a) Comparison of observations of SKS splitting (blue, red, or black) and predictions (yellow) from the 3D model of anisotropy model shown in Fig. 3a-c, where the fast direction and splitting times are summarized by the orientation and length of the bars. The blue, red, and black colors of the observed measurements identify differences with the model predictions of the fast axis directions: Blue: 0º-30º, Red: 30º-60º, Black: 60º-90º. (b)-(c) Histogram of differences between the observed and predicted fast axis directions and splitting times shown in (a). (d) Histogram of differences in anisotropy fast directions between the crust and uppermost mantle. (e) Same as (d), but for differences in fast directions between the uppermost mantle and asthenospheric layers.

Table 1. Summary of model performance.

	Variance reduction relative to an isotropic model		Comparison between predicted and observed SKS fast directions	
	Surface wave data	SKS splitting data	Standard deviation	Percentage within 20°
Model A: Crust & 220 km thick uppermost mantle	94%	36%	29°	57%
Model B: Crust, 80 km thick uppermost mantle, with a laterally homogeneous asthenosphere	94%	58%	22°	77 %
Model C: Crust, 80 km thick uppermost mantle, with a smoothly varying asthenosphere	94%	64%	18°	82%

Supplementary Materials

SM1. Misfit: To constrain the asthenospheric layer, we seek to minimize the misfit between model-predicted and observed SKS measurements defined as follows,

$$misfit = \sum_{i=1}^{N} \left[\left((\delta t_i sin2\Psi_i)_{observed} - (\delta t_i sin2\Psi_i)_{predicted} \right)^2 + \left((\delta t_i cos2\Psi_i)_{observed} - (\delta t_i cos2\Psi_i)_{predicted} \right)^2 \right]$$

where δt and Ψ are azimuthally averaged apparent splitting parameters (split time and fast axis direction, respectively) and *N* is the number of SKS measurements.

SM2. Directional correlation & statistical significance of two directional distributions: We define the directional correlation coefficient, r_{ab}, between two directional distributions $\hat{a}_i$ and $\hat{b}_i$ ($i=1,\ldots,N$) as

$$r_{ab} = \frac{\sum_{i=1}^{N} (\hat{a}_i - \langle \hat{a} \rangle) \cdot (\hat{b}_i - \langle \hat{b} \rangle)}{\sqrt{\sum_{i=1}^{N} (\hat{a}_i - \langle \hat{a} \rangle)^2} \sqrt{\sum_{i=1}^{N} (\hat{b}_i - \langle \hat{b} \rangle)^2}} \quad (1)$$

where $\hat{a}_i$ and $\hat{b}_i$ are unit vectors. Considering the 180° periodicity of fast directions, the azimuth of each fast direction is first multiplied by 2 before inserting into eq. (1), which leads to $\boldsymbol{r}$ = +1 and -1 when the distributions are parallel and perpendicular, respectively. The statistical significance of the directional correlation coefficient is assessed by Monte Carlo simulation. Although the N in eq. (1) is generally quite large (>400) due to the fine spatial grid used and the small spacing between SKS measurements, we estimate the number of independent fast direction measurements is estimated to be around 50 considering the area of our study region (~2,000,000

km^2) and our lateral resolution (~200km). In each realization of the Monte Carlo simulation, we calculate the correlation coefficient between two distributions each with 50 fast directions randomly distributed between 0° and 90°. The simulation is repeated 10^8 times and the resulting set of correlation coefficients define the probability that a measured correlation coefficient results by pure chance.

Figure S1. (a)-(b) Comparison between the 26s period Rayleigh wave azimuthal anisotropy inverted separately with ambient noise and earthquake data. (c) Earthquake results replotted only at locations where amplitudes are larger than 0.5%, to contrast with ambient noise results. Color-coding identifies differences between the earthquake and ambient noise fast axis directions: Blue: 0º-30º, Red: 30º-60º, Black: 60º-90º. General similarity is observed between the earthquake and ambient noise fast directions, with differences mostly near the periphery of the maps (Northern California to Southern Oregon) and in regions with particularly sharp isotropic velocity gradients (Northern Oregon to Southern Washington, central California). (d) Histogram of differences between ambient noise and earthquake determined fast axis directions (shown in (c)). (e)-(f) Histograms of differences in the fast axis directions and in the amplitude anisotropy between the ambient noise and earthquake results normalized by their estimated uncertainties. If the uncertainty estimates are accurate, both histograms would be Gaussian with $\sigma = 1$. This indicates that our uncertainty estimates are slightly underestimated.

Figure S2. The reduced chi-squared value, χ^2, between the observed and predicted anisotropic dispersion curves based on our crustal and uppermost mantle model at each location.

Figure S3. (a)-(d) The estimated uncertainty of azimuthal anisotropy in the crust and uppermost mantle. A grid search is performed over the four anisotropy parameters where all models with a reduced chi-squared value less than $1.5\chi^2_{best}$ are considering as acceptable. χ^2_{best} is the best fitting reduced chi-squared value shown in Fig. S2. The uncertainty for each parameter is determined by the maximum difference between the acceptable models and the best fitting model. Other than regions near the coast, anisotropic amplitude uncertainties average ~0.5% for both the crust and uppermost mantle. Uncertainties in the fast directions generally are smaller than 20º at locations with meaningful anisotropic amplitudes. Uncertainties are largest near transition regions.

Figure S4. The estimated fast direction uncertainties of anisotropy in the asthenospheric layer shown in Fig. 3c. For each location, we assume 50 independent SKS measurements are used to constrain the best fitting fast direction φ_{best} in the asthenospheric layer and the uncertainty of each SKS splitting fast direction measurement is equal to the standard deviation $\delta\theta_{best}$ of the differences between the predicted and observed SKS fast directions for the best fitting case. Based on chi-square analysis, for a model with a fast direction φ to be correct, there should be 75% chance that the predicted and observed SKS fast directions should have standard deviation $\delta\theta$ smaller than $1.06\delta\theta_{best}$. We consider all the fast direction φ satisfying this criterion to be acceptable and assign the maximum difference between the best and acceptable fast directions to be the uncertainty of φ_{best}. The largest uncertainties are coastal, particularly in Cascadia.

Figure S5. Same as Fig. 4a-c, but for Model A which only includes anisotropy in the crust and uppermost mantle layers (shown in Fig. 3a-b). The uppermost mantle thickness is extended to 220 km to minimize the misfit between the predicted and observed SKS splitting measurements. The directional correlation coefficient between the model predicted and observed SKS fast directions is $\boldsymbol{r} = 0.51$. Only one out of one million random directional distribution pairs would have a better correlation (Supplementary Materials SM2).

Figure S6. (a)-(c) Same as Fig. 4a-c, but fore Model B that has a constant fast direction (15° N of E) in the asthenospheric layer throughout the entire region. The misfit improvement relative to the model without an asthenospheric layer (Fig. S5) is significant (a 34% variance reduction), although only two parameters (fast axis direction and split time) define the asthenospheric model across the entire region. This supplies strong evidence for the existence of a deeper asthenospheric anisotropy layer that is probably significantly less heterogeneous laterally than the shallower layers of anisotropy.

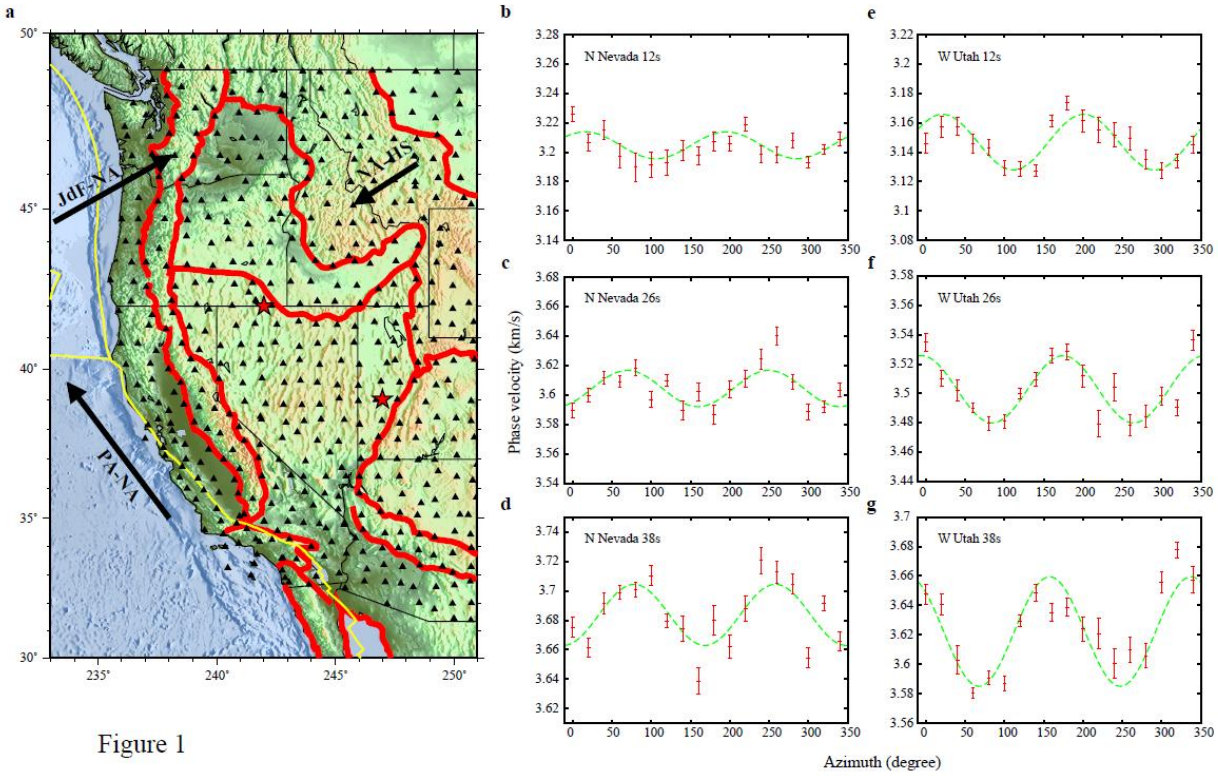
a
b
c
d
e
f
g
JdF-NA
PA-NA
SHTNS
N Nevada 12s
N Nevada 26s
N Nevada 38s
W Utah 12s
W Utah 26s
W Utah 38s
Phase velocity (km/s)
Azimuth (degree)

Figure 1

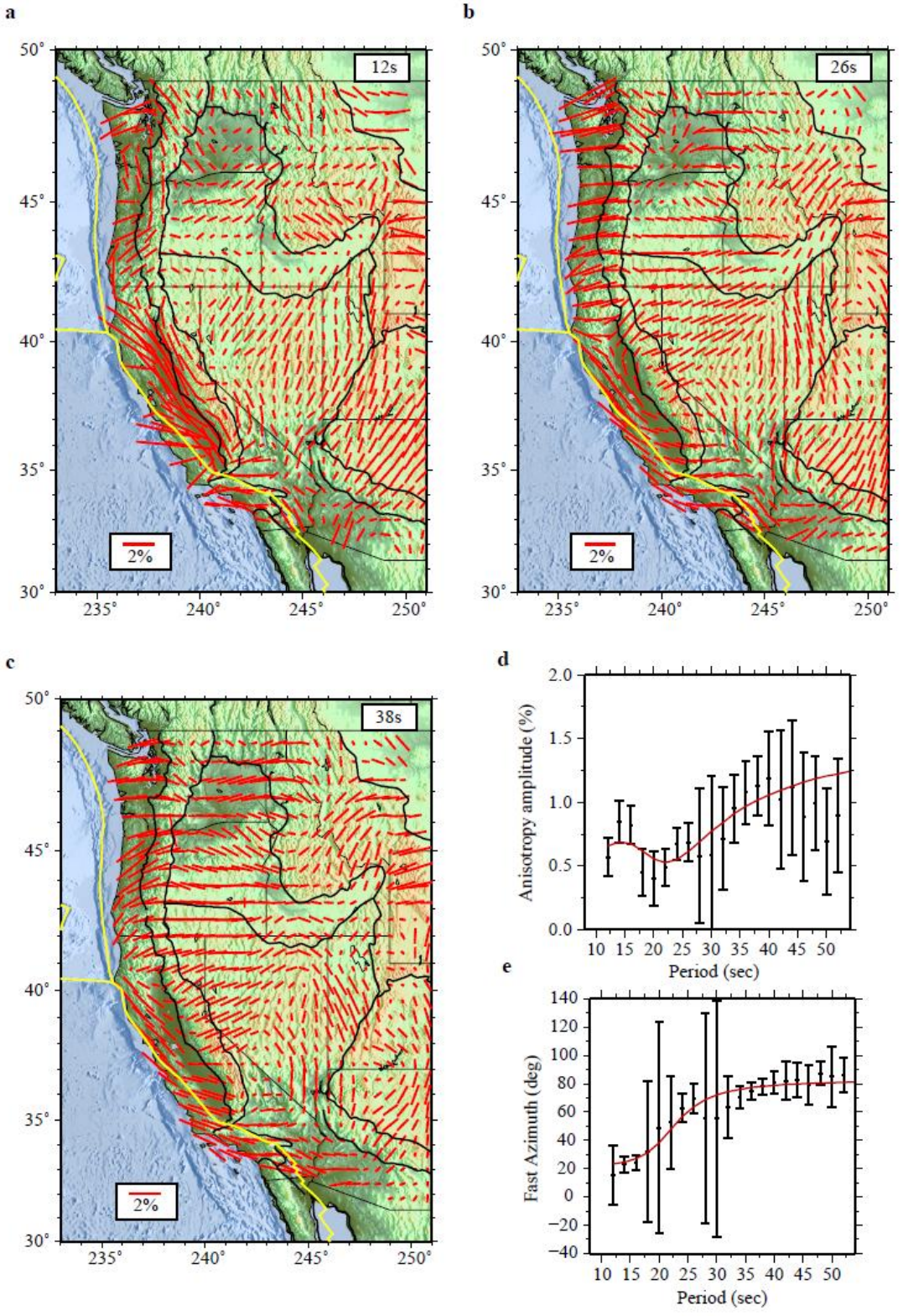
a
12s
2%
b
26s
2%
c
38s
2%
50°
45°
40°
35°
30°
235°
240°
245°
250°
d
Anisotropy amplitude (%)
2.0
1.5
1.0
0.5
0.0
10 15 20 25 30 35 40 45 50
Period (sec)
e
Fast Azimuth (deg)
140
120
100
80
60
40
20
0
−20
−40
10 15 20 25 30 35 40 45 50
Period (sec)

Figure 2

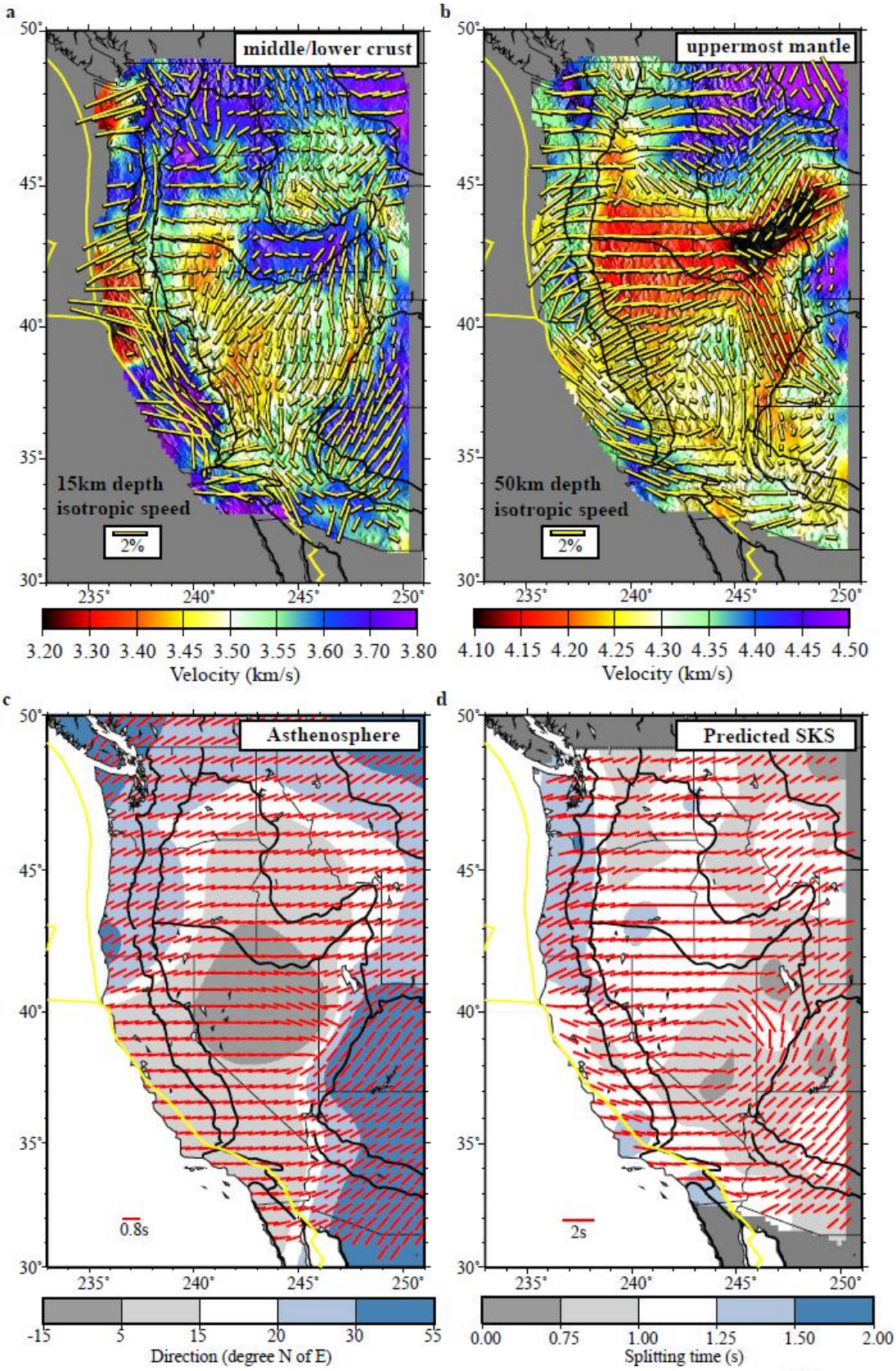
a
middle/lower crust
15km depth
isotropic speed
2%
3.20 3.30 3.40 3.45 3.50 3.55 3.60 3.70 3.80
Velocity (km/s)
b
uppermost mantle
50km depth
isotropic speed
2%
4.10 4.15 4.20 4.25 4.30 4.35 4.40 4.45 4.50
Velocity (km/s)
c
Asthenosphere
0.8s
-15 5 15 20 30 55
Direction (degree N of E)
d
Predicted SKS
2s
0.00 0.75 1.00 1.25 1.50 2.00
Splitting time (s)
50°
45°
40°
35°
30°
235°
240°
245°
250°

Figure 3

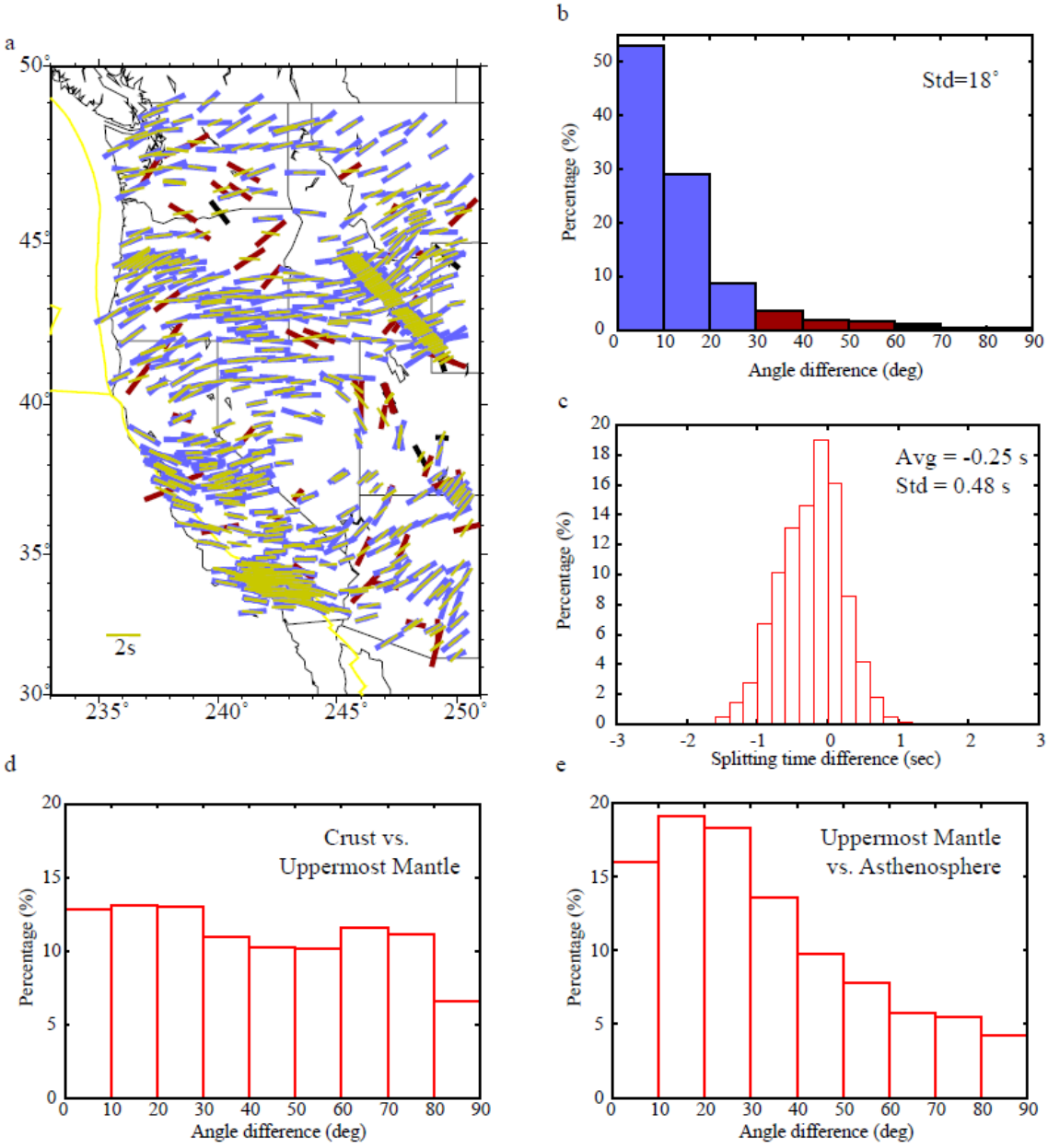
a
50°
45°
40°
35°
30°
235°
240°
245°
250°
2s
b
Std=18°
Percentage (%)
Angle difference (deg)
c
Avg = -0.25 s
Std = 0.48 s
Percentage (%)
Splitting time difference (sec)
d
Crust vs.
Uppermost Mantle
Percentage (%)
Angle difference (deg)
e
Uppermost Mantle
vs. Asthenosphere
Percentage (%)
Angle difference (deg)

Figure 4

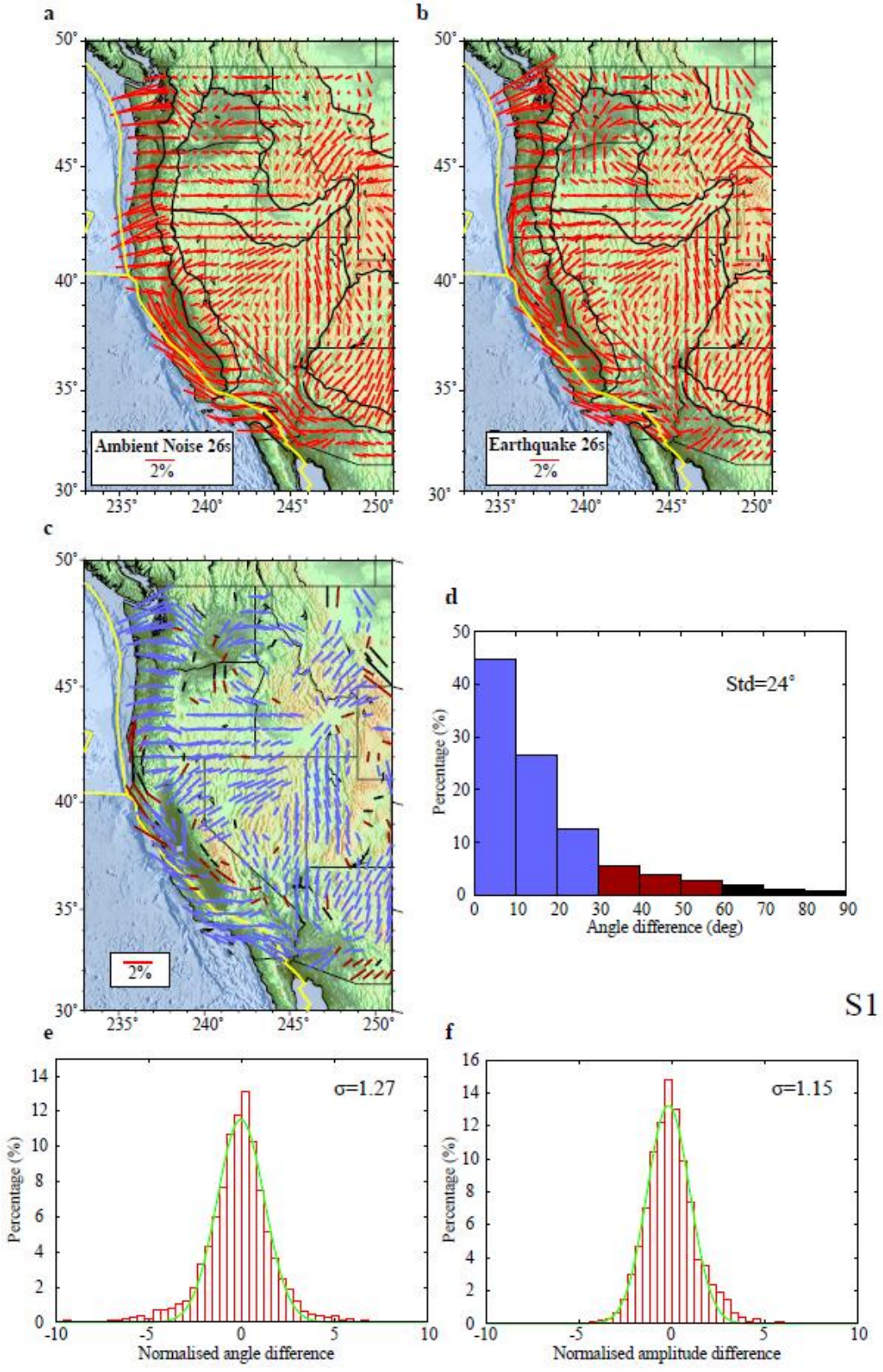
a
b
c
d
e
f
Ambient Noise 26s
2%
Earthquake 26s
2%
2%
Std=24°
Angle difference (deg)
Percentage (%)
σ=1.27
Normalised angle difference
σ=1.15
Normalised amplitude difference

S1

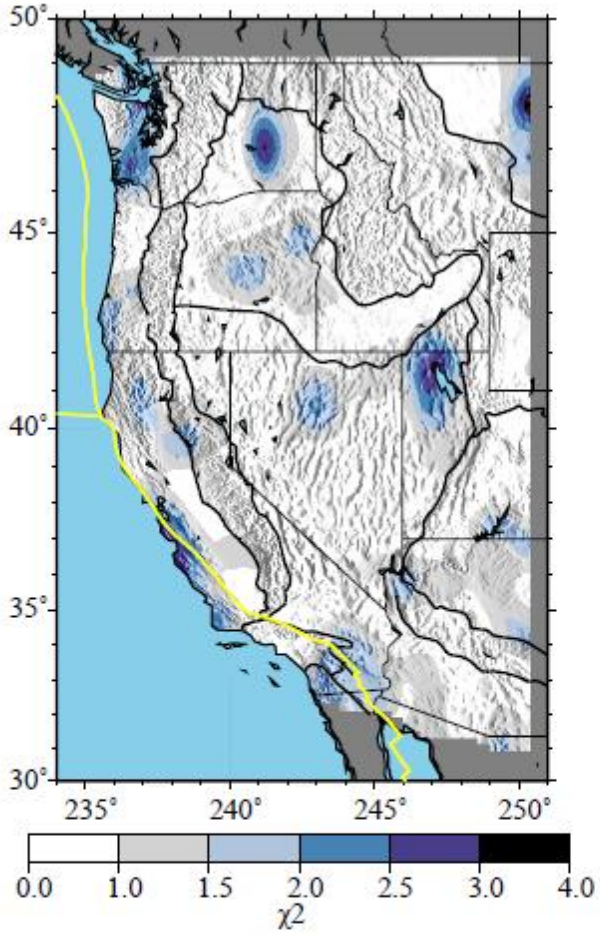
50°
45°
40°
35°
30°
235°
240°
245°
250°
0.0
1.0
1.5
2.0
2.5
3.0
4.0
χ2

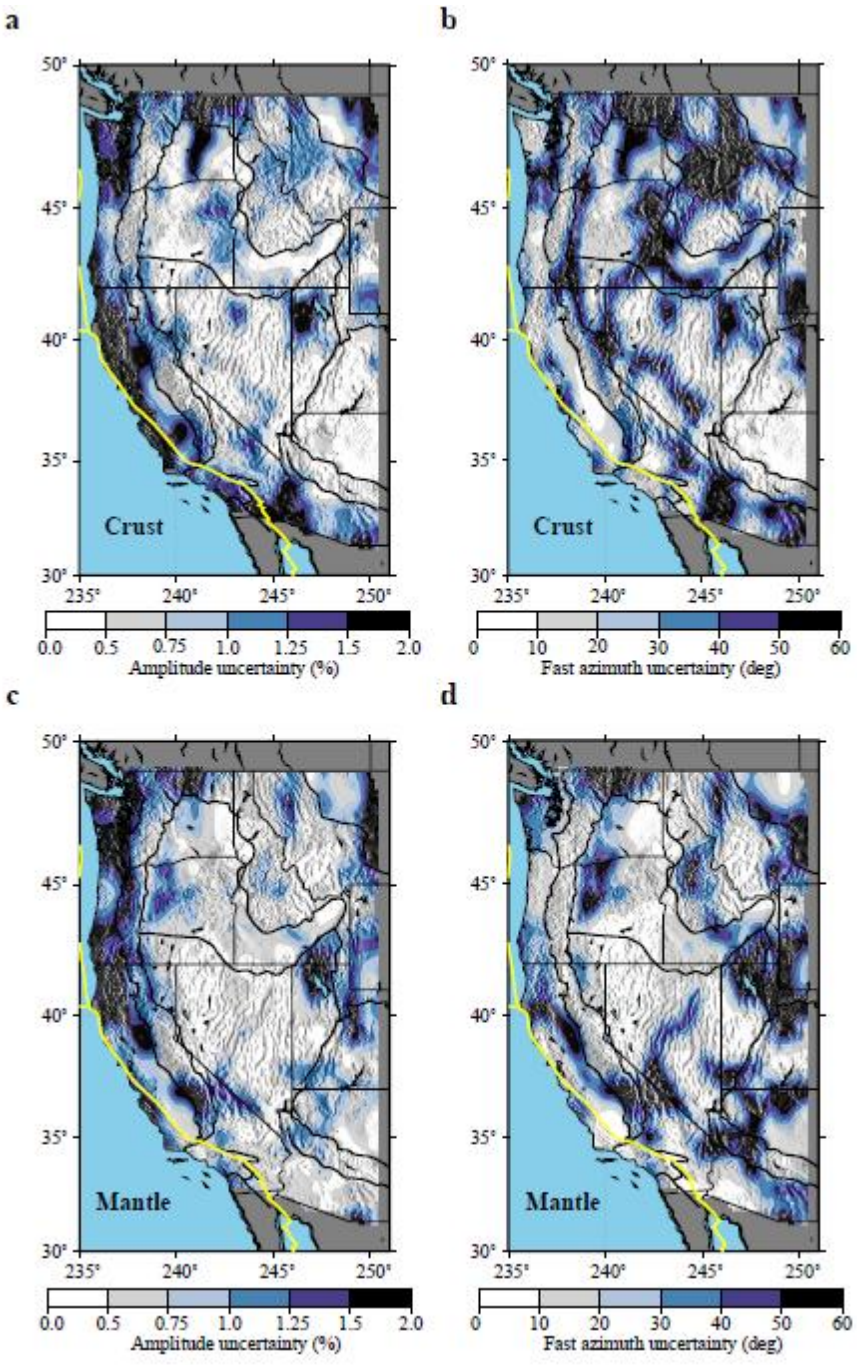
a
b
c
d
50°
45°
40°
35°
30°
235°
240°
245°
250°
Crust
Mantle
0.0 0.5 0.75 1.0 1.25 1.5 2.0
Amplitude uncertainty (%)
0 10 20 30 40 50 60
Fast azimuth uncertainty (deg)

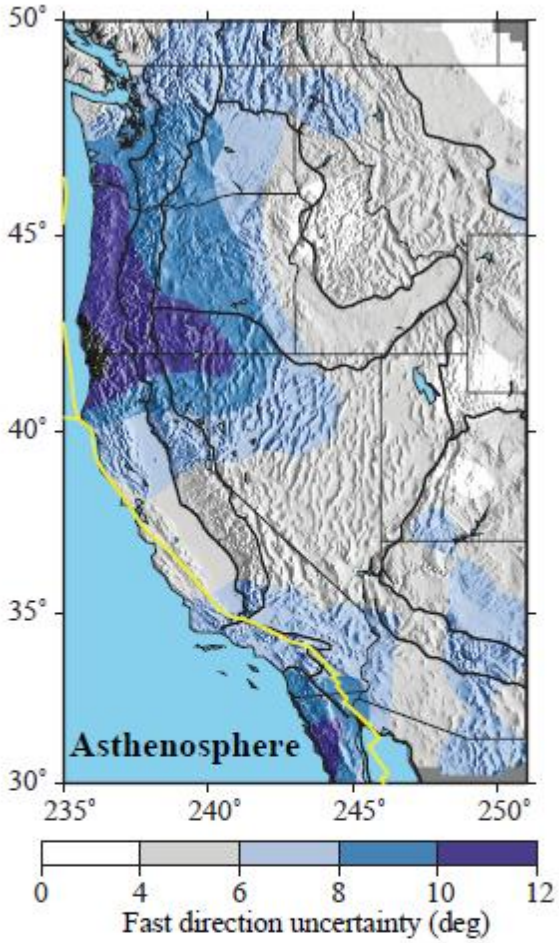
50°
45°
40°
35°
30°
235°
240°
245°
250°
Asthenosphere
0
4
6
8
10
12
Fast direction uncertainty (deg)

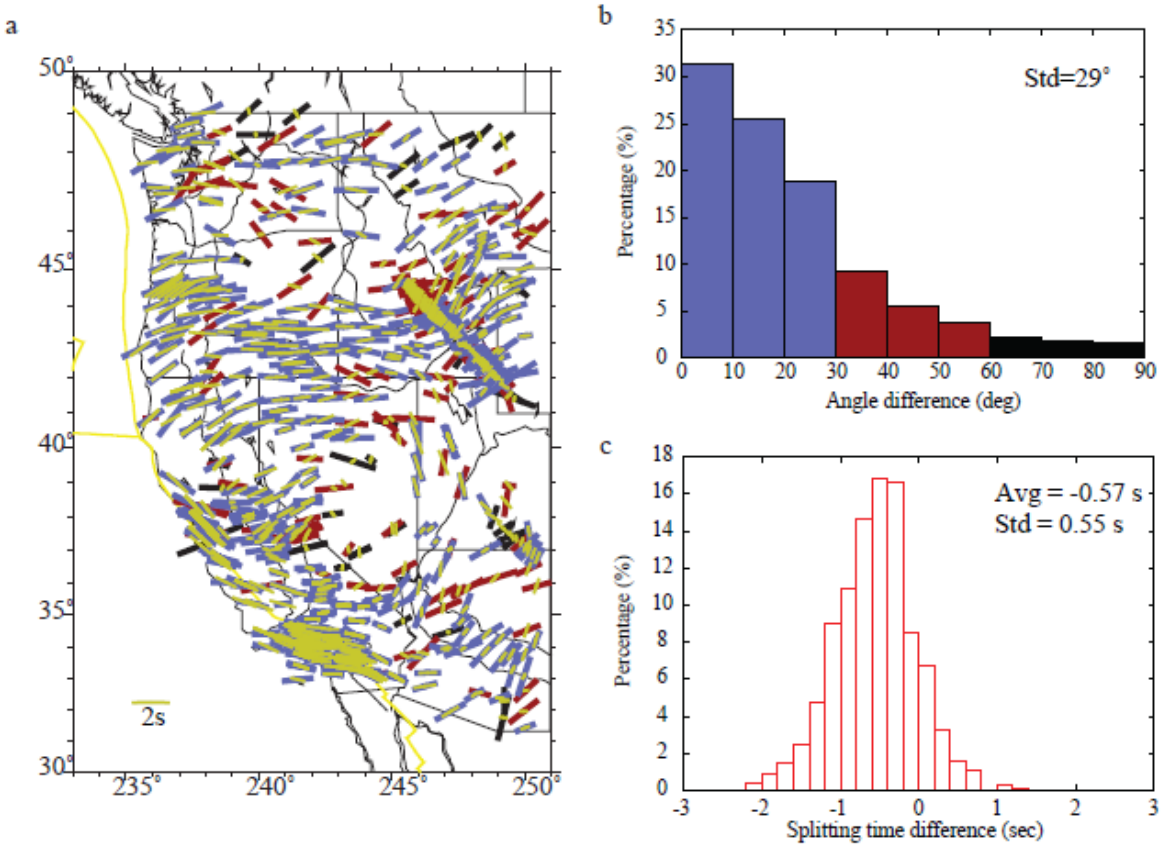
a
50°
45°
40°
35°
30°
235°
240°
245°
250°
2s
b
Std=29°
Percentage (%)
Angle difference (deg)
c
Avg = -0.57 s
Std = 0.55 s
Percentage (%)
Splitting time difference (sec)

S5

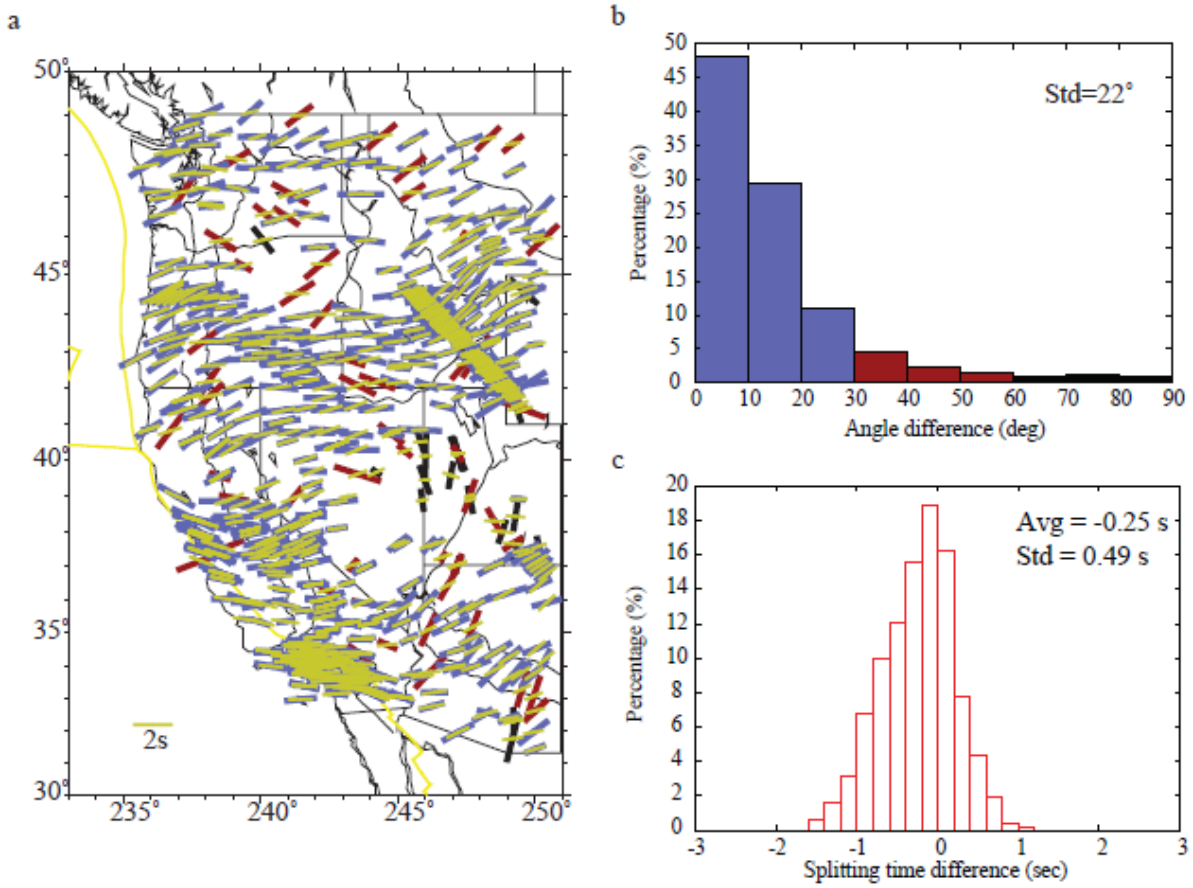
a
50°
45°
40°
35°
30°
235°
240°
245°
250°
2s
b
Std=22°
Percentage (%)
Angle difference (deg)
c
Avg = -0.25 s
Std = 0.49 s
Percentage (%)
Splitting time difference (sec)